

InGaN Quantum Dot Superlattices as Ratchet Band Solar Cells

Luc Robichaud  and Jacob J. Krich 

Abstract—In this article, we investigate the construction of ratchet band solar cells using InGaN quantum dots. The strong piezoelectric potentials can spatially separate electron and hole states. This spatial separation reduces both radiative and nonradiative recombination within the quantum dot, providing one of the key characteristics of a ratchet band system. Ratchet band solar cells have proven difficult to realize experimentally, and the piezoelectric potential in InGaN quantum dots could provide a spatial ratchet that can operate at room temperature with broadband absorption. We use a $k\cdot p$ model to calculate the electronic structure and absorbance of a superlattice of InGaN/GaN quantum dots. We present an improved method to calculate the absorbance for the bound-to-continuum transition by using bulk $k\cdot p$ states to approximate the host material continuum states. We show an example dot structure that could act as a ratchet band solar cell. Using the absorbances of the quantum dot array, we calculate a detailed balance efficiency of 36% for the system. Optimizing the dot geometry and alloy fraction allows detailed balance efficiencies up to 42% but at the cost of losing the spatial ratchet.

Index Terms—Intermediate band solar cell (IBSC), quantum dot (QD), ratchet band solar cell (RBSC).

I. INTRODUCTION

THE Shockley–Queisser limit is the limiting efficiency for a solar cell with a single band gap, 31% under a 1-sun 6000-K black body [1]. Several architectures promise higher efficiencies, and multijunction devices have already surpassed the Shockley–Queisser limit. The ratchet band solar cell is one such promising system, having a 1-sun detailed balance limiting efficiency of 48.5% [2].

The ratchet band solar cell (RBSC) was originally proposed to consist of four bands: Valence (VB), intermediate (IB), ratchet (RB), and conduction (CB) [2]. Fig. 1(a) shows an RBSC, adapted for quantum dot (QD) systems by including a VB offset. Two key features make RB systems highly efficient.

Manuscript received August 23, 2021; revised October 22, 2021; accepted January 11, 2022. This work was supported by Ontario Early Researcher Award and NSERC CREATE TOP-SET program, under Award 497981. An earlier version of this paper was presented in part at the 2021 IEEE 48th Photovoltaic Specialists Conference (PVSC) [DOI: 10.1109/PVSC43889.2021.9518410]. (Corresponding author: Luc Robichaud.)

Luc Robichaud is with the Department of Physics, University of Ottawa, Ottawa, ON K1N 6N5, Canada (e-mail: lrobi019@uottawa.ca).

Jacob J. Krich is with the Department of Physics, University of Ottawa, Ottawa, ON K1N 6N5, Canada, and also with the School of Electrical Engineering, Computer Sciences, University of Ottawa, Ottawa, ON K1N 6N5, Canada (e-mail: jkrich@uottawa.ca).

Color versions of one or more figures in this article are available at <https://doi.org/10.1109/JPHOTOV.2022.3143461>.

Digital Object Identifier 10.1109/JPHOTOV.2022.3143461

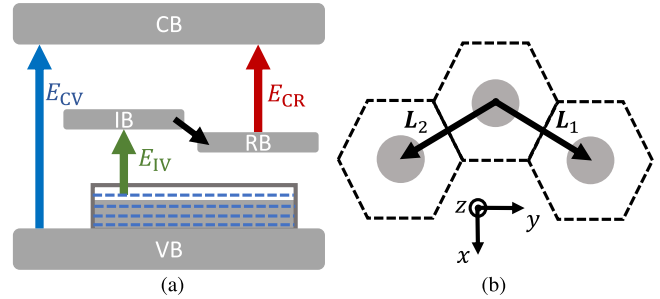


Fig. 1. (a) QD ratchet band systems, including a VB offset. Colored arrows show the energy thresholds for each transition. Carriers relax from IB to RB. (b) One plane of a hexagonal superlattice of InGaN QDs in GaN. Grey regions indicate the indium-rich regions before indium diffusion, after which there are no sharp material interfaces. L_i are the QD superlattice basis vectors. Dashed region is a superlattice unit cell.

First, recombination from the RB to the VB is forbidden so that carriers have long lifetimes in the RB after fast relaxation from the IB. The defining characteristics of an RB system are three optical transitions with threshold energies E_{CV} , E_{CI} , and E_{IV} , as indicated by the colored arrows in Fig. 1(a). The second advantageous feature is that $E_{CI} + E_{IV}$ does not need to equal E_{CV} , unlike in a standard intermediate band solar cell (IBSC) [3]. This relaxation can lead to better voltage matching between the subgap and CV transitions than in an IB system [4], [5].

While realizations of RB systems have been demonstrated using InAs QDs [6], quantum-cascade-style AlGaAs/GaAs quantum well superlattice [7], and erbium-doped GaAs [8], none has been implemented that can function at room temperature with the required broadband absorptions. We propose using InGaN QDs in GaN for RBSCs. InGaN QD systems have been of interest for IBSCs [9], [10]. Confined systems, such as QDs and wells, have electronic structures that are tunable by change of size and composition such that the optical threshold energies do not necessarily sum to the host material's band gap, as required for an RBSC [6]. InGaN QDs are also strongly piezoelectric such that the strain-driven piezoelectric potential can spatially separate the lowest confined electron and hole states [11], as illustrated in Fig. 2. This system presents a realizable spatial ratchet with optical transitions as indicated in Fig. 2, analogous to those of Fig. 1(a). Separating the states reduces the wavefunction overlap, reducing both radiative recombination and local nonradiative processes.

In this article, we construct an example of a clear ratchet (CR) band system, attainable with a 3-D superlattice of InGaN QDs in GaN. We calculate the electronic structure of the QD

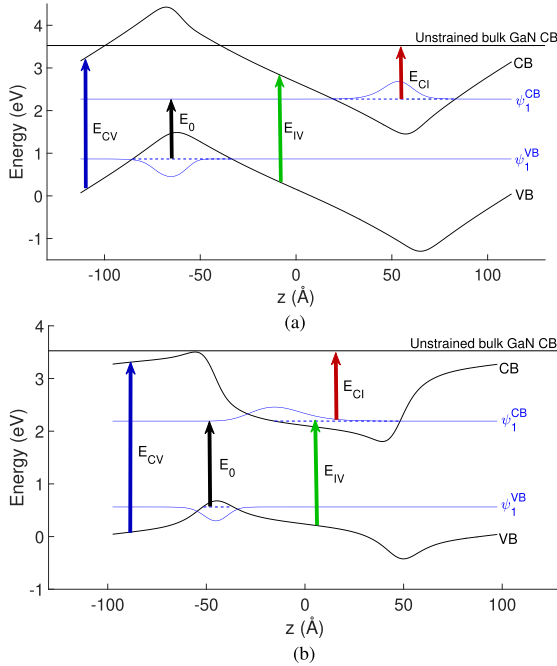


Fig. 2. Electronic structures of InGaN QD superlattices in GaN along a cut through the axis of the cylinders. (a) Clear ratchet (CR) system and (b) efficiency optimized (EO) system. Solid black lines are bulk band edges, which are modified by the piezoelectric potential and the diagonal portion of the deformation potential. Blue dashed lines are the lowest electron/hole state energies. Blue solid lines are z -axis projections of the squared wavefunctions. Note that the electron state of the CR is localized at the top of the dot and the hole at the bottom, increasing excitation lifetimes. The EO wavefunctions do not show spatial separation.

superlattice, including strain, deformation potentials, and piezoelectric potentials, using a computationally efficient symmetry adapted $\mathbf{k}\cdot\mathbf{p}$ method for cylindrical QDs that includes effects of alloy diffusion and nonuniform elastic and dielectric constants [12]. We calculate the subgap absorption cross sections of the dots and construct absorptances of systems with 1–200 QD layers and an ideal Lambertian back reflector [13], where the QD structure is doped so some IB states in the QD are filled. We find the energy thresholds corresponding to E_{IV} and E_{CI} in Fig. 1(a). We show how E_{IV} changes with doping, demonstrating the key feature of a RB system: An absorption threshold E_{IV} larger than the fundamental gap of the quantum dot system, in the limit that the doping goes to zero. For the absorption cross sections, we demonstrate an improved method for calculating bound-to-continuum absorption.

We use detailed balance calculations to determine the limiting efficiency possible for such devices, using both idealized energy thresholds and the $\mathbf{k}\cdot\mathbf{p}$ -predicted absorptances. We use this efficiency landscape to optimize the QD geometry and alloy fraction, giving an efficiency of 42%, larger than the 36% of the CR system. The efficiency-optimized (EO) system does not have a ratchet. Despite the differences in detailed balance efficiencies, in real materials with nonradiative recombination, the ratchet structure may have a higher efficiency than the EO structure because of reduced IV recombination. We also show that the efficiency of the CR system depends on having a large number

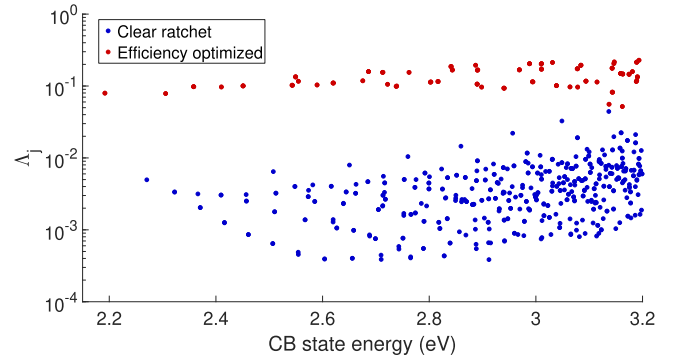


Fig. 3. Spatial overlap between electronic states with energy E and the lowest hole state, as defined by (1) for the CR (blue) and EO (red) systems. The CR system spatially separates the states significantly more than the EO system.

of QD layers, while the EO system is less sensitive, meaning we could consider a system, where we sacrifice some of the spatial ratchet so we can reduce the number of layers.

This article is an extended version of an IEEE Photovoltaics Specialists Conference Proceeding [14], which presented preliminary results on the CR system. This version adds Section IV with the detailed balance efficiency calculations for the QD system using idealized energy thresholds as well as $\mathbf{k}\cdot\mathbf{p}$ -predicted absorptances. With those efficiencies, we optimize the QD geometry and indium fraction to maximize efficiency. In addition to Section IV, this version adds Figs. 2(b), 3, 4(b), 5(b), and 7–10 and new results in Fig. 6.

II. QUANTUM DOT ELECTRONIC STRUCTURE

We use an eight-band $\mathbf{k}\cdot\mathbf{p}$ model to calculate the single-particle electronic structure of a superlattice of wurtzite InGaN QDs, which we approximate as cylindrical. We previously showed that considering hexagonal dots makes essentially no difference for the most confined energy levels [12]. To preserve the C_6 symmetry of the wurtzite crystal structure, hexagonal periodic boundary conditions are imposed, producing a 3-D QD superlattice, as illustrated in Fig. 1(b) [15], [16]. The electronic structure methods are described in [12], and we give a brief summary here. The Hamiltonian is calculated using a symmetry adapted basis, which reduces the computational cost by block diagonalizing the Hamiltonian [17], [18]. Lattice-mismatch driven strain is calculated using a continuum approximation and is included directly in the $\mathbf{k}\cdot\mathbf{p}$ model by deformation potentials [15]. The piezoelectric potential, which is crucial for generating spatially separated electron and hole states, is calculated from the strain using Maxwell's equations. Indium diffusion is incorporated by smoothing the indium profile with a Gaussian kernel of 5 Å in each direction [12]. Material parameters are the same as those used in [12] except for the sign of the e_{15} piezoelectric constant.¹ The $\mathbf{k}\cdot\mathbf{p}$ method gives well-resolved

¹There is a sign error in e_{15} in [12], which follows [19]. This widespread sign error is discussed in greater detail in the erratum [20] to [21], which implements an eight-band $\mathbf{k}\cdot\mathbf{p}$ model using a plane wave basis to describe III-N QDs. This correct sign was also confirmed using *ab initio* DFT in [22]. We thank Stanko Tomić for making us aware of this error.

energies and eigenstates for the most confined energy levels but is less accurate for the states approaching the continuum [18], [23].

In this article, we highlight two QD superlattices. The first is designed to show a CR effect, which should be experimentally measurable. These QDs have 90-Å radius, 125-Å height, and 40% indium fraction with a barrier of 100 Å between dots in both the z direction and in-plane. The resulting hexagonal superlattice unit cell has a thickness of 225 Å and hexagonal edge length of 162 Å, producing a QD areal density of $1.5 \times 10^{11} \text{ cm}^{-2}$. The barrier thicknesses were chosen to be sufficiently small to ensure strong absorption and to help with convergence of the electronic structure [12]. To resolve the states, 25 plane waves were used in the axial direction and 17 were used along each in-plane hexagonal principal axis in the reciprocal space. Note our sampling grid is not rectangular but instead truncated to have a C_6 symmetric grid [12], as is required by a symmetry adapted basis, resulting in a total of 5425 plane waves. We refer to this system as the CR. We also highlight another structure designed to optimize the detailed balance efficiency of the system. This system has dots with a 35-Å radius, 95-Å height, and 76% indium fraction. We kept the same 100-Å dot-to-dot barriers as in the CR system, resulting in a unit cell thickness of 195 Å, hexagonal edge length of 98 Å and an areal QD density of $4.0 \times 10^{11} \text{ cm}^{-2}$. To resolve the states, we found that 19 plane waves were needed along each of the axial and in-plane directions, which gave 5149 plane waves after truncation. We refer to this system as the “efficiency optimized” (EO). The optimization process that produced this structure is described in Section IV.

Fig. 2 shows the electronic structure for both systems. As usual for QD IBSCs, we consider the QD-confined states in the CB to be the IB, while the continuum states form the CB. Colored arrows show the equivalent transition energies of the ideal RBSC shown in Fig. 1(a). The IV transition moves electrons from the confined VB states to the confined IB states. In the case of the CR in Fig. 2(a), after an electron-hole pair is created via the IV transition, the electron and hole relax toward opposite ends of the dot because of the piezoelectric potential. Once relaxed, the electrons can no longer recombine because states of lower energy are either filled or spatially separated, increasing their lifetime and enabling them to wait longer for a photon for the CI transition. In the EO system of Fig. 2(b), the piezoelectric fields are weaker, and there is considerable overlap between the lowest IB and VB states; this system does not have a ratchet. We define the energy separation between the lowest hole and electron states to be E_0 . While Fig. 2 shows a cut through a single dot in the array, the QD-containing region of the full device is terminated with GaN, and the E_{CV} and E_{CI} energies must be defined by that GaN band structure, to enable extraction of carriers. We, therefore, take the CI transition to be from the IB to the CB continuum of the host GaN, which is at 3.53 eV in this article; the bandgap of GaN is 3.51 eV and the reference energy is the GaN VB edge without spin-orbit coupling and crystal-field splitting, as described in [19] and [24]. Fig. 2 shows approximate energy thresholds E_{XY} for transitions between bands. In reality, absorption for the IV and CI transitions begins at smaller energies, absorption for the IV and CI transitions begins

in detail below. The CI transition can begin at lower energy because of occupancy of higher lying states in the IB, and the IV transition can begin at lower energy because of the finite spatial extent of the bound wavefunctions. For the systems we consider, $E_{CI} + E_{IV} < E_{CV}$, as depicted in Fig. 1(a).

The spatial separation of the lowest energy states in the ratchet system can be seen in the overlap of the VB and IB wavefunctions. In Fig. 3, we investigate the overlap between the lowest hole state ψ_1^{VB} and CB states ψ_i^{CB} using the metric

$$\Lambda_i = \int d^3\mathbf{r} |\psi_1^{VB}(\mathbf{r})| |\psi_i^{CB}(\mathbf{r})| \quad (1)$$

which is bounded between 0 and 1. While all eigenstates are orthogonal, Λ_i is small when states have no spatial overlap. In the CR system, Λ_i is considerably smaller, especially for the lowest energy states, showing the spatial ratchet separating the lowest IB eigenstates from the VB ones. In both systems, Λ_i increases for higher energy CB states, which are increasingly delocalized. This effect is larger for the CR system, in which the lowest CB states have strongly reduced overlap with the lowest hole state.

These overlaps are indicative of a spatial ratchet, but not sufficient to conclude that the ratchet is functioning. The key feature of the RBSC threshold energies in Fig. 2 is that there is no IV absorption at the energy E_0 , because of the spatial separation of electron and hole states. The actual absorption threshold E_{IV} is larger than E_0 , which is essential to constructing the RB system. We now turn to calculating these thresholds quantitatively by constructing the absorption cross sections of a single dot and then the absorptances of the full dot array.

III. OPTICAL ABSORPTION

Given our interest in blocking recombination within the QD, we focus on the IV and CI subgap transitions. Since the QD $\mathbf{k}\cdot\mathbf{p}$ model describes well the bound electron and hole states, we naturally use these to calculate the absorption for the IV transition. In contrast, the CI transition reaches the continuum, for which we introduce other methods. Beginning with the IV transition, in the electric dipole approximation, we can calculate the absorption cross section between initial and final bound states $|\psi_i\rangle$ and $|\psi_f\rangle$, respectively. The relevant dipole matrix element is [17], [25],

$$M_{if} = \frac{1}{A} \langle \psi_i | \hat{H}' | \psi_f \rangle \quad (2)$$

where $\hat{H}'(\mathbf{k}) = \hat{H}(\mathbf{k} + \frac{e}{\hbar}\mathbf{A}) - \hat{H}(\mathbf{k})$ is the interaction Hamiltonian, \hbar the reduced Planck's constant, e the electric charge, and \mathbf{A} the vector potential. Here, \hat{H} is the QD $\mathbf{k}\cdot\mathbf{p}$ Hamiltonian. We only keep terms that are linear in \mathbf{A} . From these matrix elements, the absorption cross section is [17]

$$\sigma_{if}(E) = \frac{2\pi\hbar}{\bar{n}\varepsilon_0 c E} |M_{if}|^2 (f_i - f_f) g(E_f - E_i - E) \quad (3)$$

where \bar{n} is the average refractive index, ε_0 the vacuum permittivity, c the speed of light, f_i the Fermi-Dirac distribution at

energy E_i , and

$$g(E) = \frac{1}{\Delta\sqrt{2\pi}} \exp\left(-\frac{E^2}{2\Delta^2}\right) \quad (4)$$

represents inhomogeneous broadening due to variation in QD sizes, which is controlled by the parameter Δ . The total absorption cross section for the bound-to-bound approach can then be obtained by summing over all possible transitions

$$\sigma_{\text{BB}}(E) = \sum_{if} \sigma_{if}(E) \quad (5)$$

where i and f both run over all states in the VB, IB, and CB, although only occupied states contribute to i and unoccupied states contribute to f . In what follows, all cross sections are calculated using a temperature of 300 K. Based on photoluminescence measurements, the inhomogeneous broadening from self-assembled QDs ranges widely from 20–200 meV depending on temperature, growth, and the number of QD layers [26]–[28]. Calculations assume $\Delta=20$ meV unless otherwise specified, and we show the sensitivity of the device efficiency and ratchet to Δ .

The CI process involves transitions to higher energy continuum states that are not necessarily well resolved in the $\mathbf{k}\cdot\mathbf{p}$ model, which is best at capturing the lower energy states, which require fewer plane waves. In this case, it is preferable to approximate the continuum states using a model in which they are well described [23], [29], [30]. Tomić *et al.* [23] approximated the continuum states as CB plane waves with a parabolic dispersion. Since we work within the $\mathbf{k}\cdot\mathbf{p}$ framework, we can easily describe the continuum states as the bulk states of the $\mathbf{k}\cdot\mathbf{p}$ model of GaN. These states are modified plane waves that include mixing between the eight bands of the $\mathbf{k}\cdot\mathbf{p}$ model and nonparabolicity of the dispersion, with all effects kept to the same order of approximation as for the bound states. The states from this approach should better capture the high energy states in the QD array than a simple effective mass approximation for the plane wave states. It is then a simple matter to calculate transition dipole matrix elements from the bound states to the bulk GaN states. As with the standard bound-to-free calculation, this approximation for the free states assumes that the continuum states are only lightly perturbed by the presence of the QD, which becomes more accurate at higher energy.

Under this approximation, we take the dipole matrix elements from bound state $|\psi_i\rangle$ to free state $|\psi(\mathbf{k})\rangle$ to be

$$M_i(\mathbf{k}) = \frac{1}{A} \langle \psi_i | \hat{H}' | \psi(\mathbf{k}) \rangle. \quad (6)$$

The continuum states $|\psi(\mathbf{k})\rangle$ are eigenstates of a bulk GaN Hamiltonian whose material parameters are independent of space; the states are normalized to the volume of the superlattice unit cell to give the proper matrix element [23]. The material parameters contained in the interaction Hamiltonian \hat{H}' vary spatially according to the alloy profile of the QD superlattice. The cross section $\sigma_i(E, \mathbf{k})$ is calculated from $M_i(\mathbf{k})$ similarly to (3), and the associated total absorption cross section is [23]

$$\sigma_{\text{BC}}(E) = \frac{V}{(2\pi)^3} \sum_i \int d^3\mathbf{k} \sigma_i(E, \mathbf{k}) \quad (7)$$

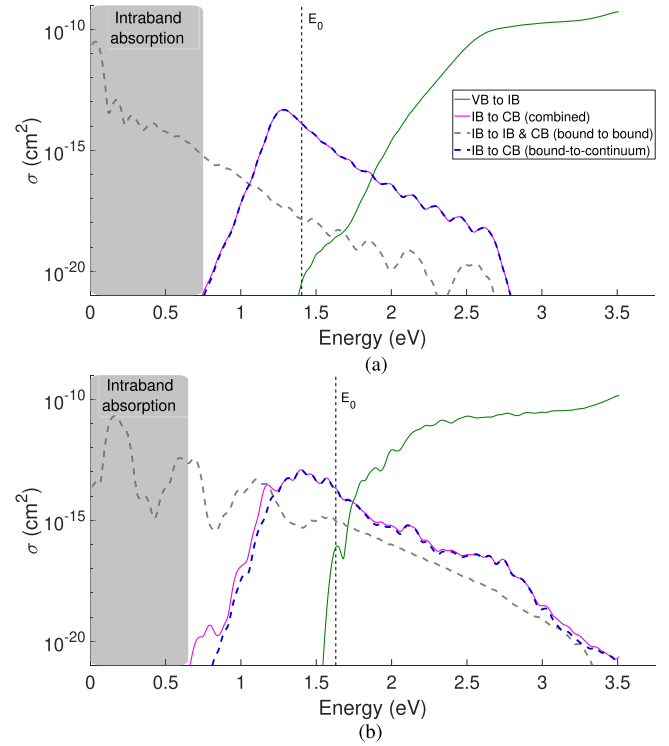


Fig. 4. Absorption cross sections calculated using the bound-to-bound, bound-to-continuum, and combined approaches for (a) CR system and (b) EO system. In the CR system, the combined result for σ_{CI} overlaps with the bound-to-continuum result. Regions in grey represent intraband absorption that do not contribute to current generation. Vertical dashed lines show E_0 as defined in Fig. 2. Fermi level is fixed such that there are 4.9 electrons in each QD for the CR system and 6.1 for the EO.

where V is the volume of the QD superlattice unit cell. The integral in (7) is calculated directly in the \mathbf{k} -space used for the $\mathbf{k}\cdot\mathbf{p}$ calculations.

Fig. 4 shows the 300-K cross sections obtained from both bound-to-bound and bound-to-continuum calculations. To ensure that both subgap optical transitions can occur, we consider the Fermi level to be fixed to give six electrons per QD if the temperature were 0 K. At 300 K, this Fermi level gives 4.9 electrons per QD in the CR and 6.1 electrons per QD in the EO and correspond to doping in the QD region of the device of approximately $3 \times 10^{17} \text{ cm}^{-3}$ for the CR and 10^{18} cm^{-3} for the EO system. The bound-to-bound calculations for IV and CI transitions consider all possible pairs of bound states corresponding to each transition. Since the IB and CB are both formed from the conduction band states of the original materials, the cross sections labeled as CI include absorptions that can also be thought of as being intraband transitions within the IB; that is, the final state is below the 3.53-eV GaN CB level, so they do not produce carriers that can be collected. This range of energies is highlighted in Fig. 4 in grey and is not relevant for device operation.

For absorptions that end with an electron above the barrier-material CB edge, which can produce current, the bound-to-continuum calculation initially underestimates the cross section,

as it underestimates the density of receiving states at the threshold. On the other hand, at higher energies, the bound-to-bound calculation considerably underestimates absorption for the CI transition as it is computationally costly to include sufficient plane waves to resolve the free states; in both cases, the larger value is more accurate as it has better sampling over the receiving states. We combine the reliable portions of both methods by adding σ_{BC} to the portion of σ_{BB} in which the final states have energy above the 3.53-eV GaN CB energy level, making the resulting carriers capable of being collected. With this restriction, only a portion of the transitions that produce the grey line also contribute to the CI cross section, and the combined line (magenta) is not simply the sum of the blue and grey lines. For the CR device, this combined method (magenta) is nearly on top of the bound-to-continuum method (blue), showing that the bound-to-continuum alone is sufficient for calculating the cross section. For the EO device, however, the bound-to-bound calculation causes a more significant change at low energy, reducing E_{CI} compared with where it would be with only the bound-to-continuum model.

Fig. 4 makes clear that both systems display broadband subgap absorption, which has been a challenge in other ratchet band implementations. Note in particular that σ_{IV} for the EO system rises much more rapidly than with the CR. The spatial separation of states in the CR reduces the optical absorption, which is part of why the CR does not have the highest detailed balance efficiency, as is shown in Section IV. However, the CR should have reduced IV recombination compared with the EO.

We move from the individual dot to the absorbance of the full array by considering the effective absorption coefficient $\alpha(E)$ of the QD material for normally incident light, with each dot treated independently

$$\alpha(E) = \rho\sigma(E) \quad (8)$$

where ρ is the volumetric density of dots. To achieve strong absorption, we consider the statistical light-trapping limit [13], in which the absorbance is

$$a(E) = \frac{4\bar{n}^2\alpha(E)N_L L_3}{4\bar{n}^2\alpha(E)N_L L_3 + 1} \quad (9)$$

where N_L is the number of layers of dots and L_3 is the height of a supercell in the z-direction.

The key feature of a ratchet band is having the absorption threshold for the IV process be at energy larger than E_0 , the fundamental gap of the system. We begin by considering a strongly absorbing system with 200 layers of QDs. The system has a ratchet regardless of whether such a large number of dot layers is considered, as we show below. We observe the ratchet effect in Fig. 5(a), in which E_{IV} is 0.46 eV above E_0 . Here, we define E_{IV} and E_{CI} as the lowest energy at which their respective absorbances equal 1%. We choose the number of plane waves to converge E_{IV} within 3 meV and E_{CI} within 2 meV.

We must rule out this shift occurring because of the doping of the QDs, which fills the lowest IB states and blueshifts the IV absorption edge solely by Pauli exclusion. To rule out this mundane effect, Fig. 6 shows how the absorption edge E_{IV} shifts

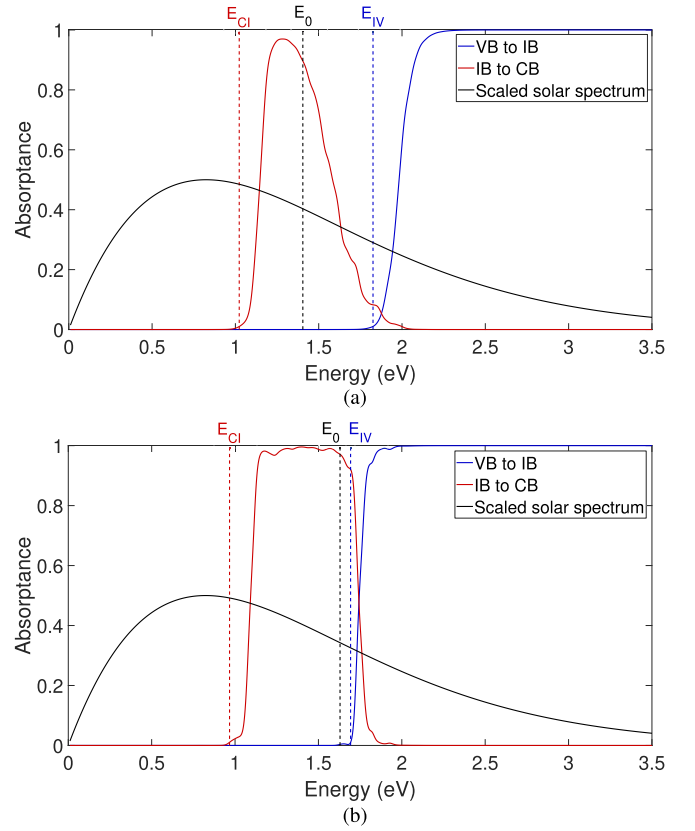


Fig. 5. Absorbances for the two subgap transitions calculated from the k - p model with 200 layers of QDs for (a) CR system and (b) EO system. Absorbances for the CI transition were calculated from the combined approach, detailed in the text. Black vertical dashed line is E_0 , as shown in Fig. 2. Blue and red vertical dashed lines are the energy thresholds for the IV and CI transitions, respectively. Temperature is 300 K and the Fermi level is fixed such that there are 4.9 electrons in each QD for the CR system and 6.1 for the EO. While the CR shows a clear difference between E_{IV} and E_0 , the optimized system also seems to present at most a small ratchet. While the offset between E_{IV} and E_0 in (a) is a true ratchet, the offset in panel (b) is due to electron filling of the CB states, as shown in Fig. 6. Black solid lines show scaled photon flux of a 6000-K black body, for reference.

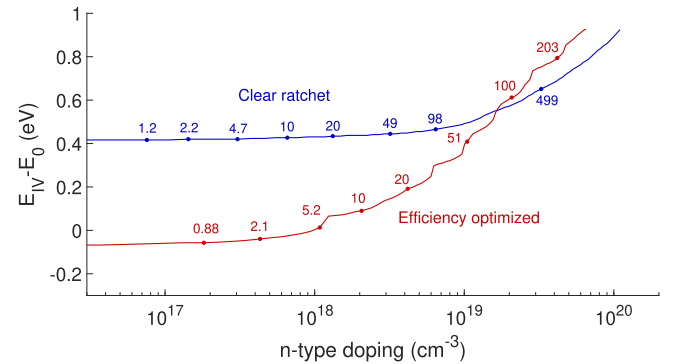


Fig. 6. IV transition energy threshold E_{IV} relative to E_0 for the CR (blue) and EO (red) systems. Temperature is 300 K and the numbers along curves indicate the mean number of electrons per QD at selected dopings. For the CR system, E_{IV} is above E_0 as IB doping is reduced to zero. This blueshift of E_{IV} relative to E_0 is due to the spatially separated electron and hole states. In the case of the EO system (red), E_{IV} settles slightly below E_0 , which indicates that there is no ratchet. E_{IV} goes below E_0 because of our definition of the absorption edge and linewidth broadening of the absorption.

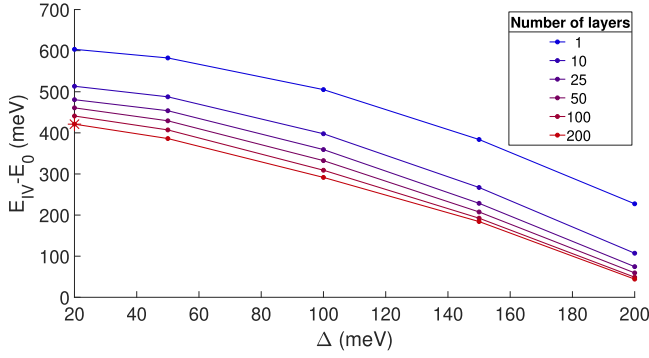


Fig. 7. IV transition energy threshold E_{IV} relative to E_0 as function of linewidth broadening Δ for the CR system. Different curves are for varying number of layers of QDs. Star marker indicates the default parameters of $\Delta=20$ meV and $N_L=200$ used unless otherwise specified. EO system has no spatial ratchet, as determined from Fig. 6 and is, therefore, not shown. Temperature is 300 K and the Fermi level is such that there are 4.9 electrons per QD.

with doping. We see that in the CR system, E_{IV} remains blue shifted from E_0 as the doping becomes small, ruling out Pauli exclusion effects. We conclude that we have a true RB system, driven by the spatial separation of the electron and hole states. By contrast, in the EO system, in the limit of an empty IB, E_{IV} reaches E_0 and in fact is slightly below E_0 because of the linewidth broadening Δ , showing that there is no spatial ratchet. Fig. 6 was obtained with $\Delta=20$ meV, which is on the optimistic side of the broadening range. Fig. 7 shows that the CR system continues to have a ratchet all the way up to 200 meV, although it is more prominent for smaller Δ . Because E_{IV} is determined by the system's absorptance, as would be easy to measure experimentally, decreasing the number of QD layers blueshifts E_{IV} , increasing the ratchet energy $E_{IV} - E_0$. The ratchet may, therefore, be more readily observable in systems with fewer layers.

IV. EFFICIENCIES

To calculate the limiting power conversion efficiency of the system, we use detailed balance calculations as previously described [5], [31]. The photon fluxes absorbed by or emitted from transitions between bands X and Y from the sun, solar cell, and ambient are given by a modified Planck spectrum [32]

$$\phi_{XY}(\mu_{XY}, T) = \frac{2\pi}{h^3 c^2} \int_0^\infty dE \frac{a_{XY}(E) E^2}{e^{(E-\mu_{XY})/kT} - 1} \quad (10)$$

where μ_{XY} is the quasi-Fermi level splitting between bands X and Y , k is the Boltzmann constant, T the temperature, and a_{XY} is the absorptance between bands X and Y . We consider photons with energy larger than the CV bandgap of 3.53 eV to be exclusively absorbed by the CV transition, before they reach the IB region of the device. For energies at which both IV and CI processes can absorb

$$a_{XY} = a_{\text{tot}} \frac{\alpha_{XY}}{\alpha_{CI} + \alpha_{IV}} \quad (11)$$

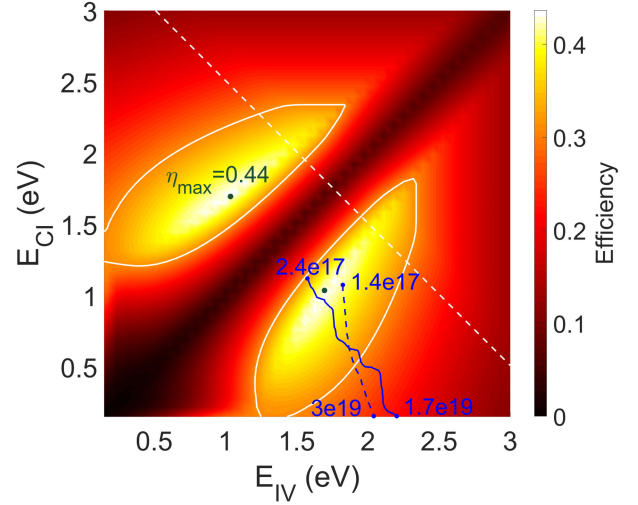


Fig. 8. RBSC detailed balance efficiency for a GaN host material under a 1-sun black-body spectrum. White contour is the Shockley–Queisser limit. Overlaid on the color plot are two trajectories showing the attainable energy thresholds for the CR (dashed) and EO (solid) systems, as the doping of the QDs varies. Annotations at line extremities indicate n-type doping in cm^{-3} to achieve those energy thresholds. White dashed line represents the IBSC, where $E_{IV} + E_{CI} = E_{CV}$. The optimal efficiency occurs where $E_{IV} + E_{CI} < E_{CV}$, giving the device more current while reducing its voltage.

where a_{tot} is calculated from (9) with $\alpha = \alpha_{CI} + \alpha_{IV}$. Under the usual detailed balance assumptions of only radiative recombination, infinite carrier mobility, that each absorbed photon produces one electron–hole pair, and no current from the QD bound states, the extracted current is

$$J = q (\dot{N}_{CV} + \dot{N}_{CI}) \quad (12)$$

where

$$\begin{aligned} \dot{N}_{CI} &= C f_s \phi_{CI}(0, T_s) + (1 - C f_s) \phi_{CI}(0, T_a) - \phi_{CI}(\mu_{CI}, T_a) \\ \dot{N}_{CV} &= C f_s \phi_{CV}(0, T_s) + (1 - C f_s) \phi_{CV}(0, T_a) \\ &\quad - \phi_{CV}(\mu_{CV}, T_a) \end{aligned}$$

where C is the concentration factor, $T_a = 300$ K is the ambient temperature, $T_s = 6000$ K is the solar temperature, and $f_s = 2.16 \times 10^{-5}$ is the angular size of the sun. We take $C = 1$ for a 1-sun concentration.

We consider two cases of absorptances, with the first being the ideal perfectly nonoverlapping absorptions [3], where

$$a_{CI}(E) = \Pi_{E_{CI}}^{E_{IV}}(E) \quad (13)$$

$$a_{IV}(E) = \Pi_{E_{IV}}^{E_{CV}}(E) \quad (14)$$

$$a_{CV}(E) = \Pi_{E_{CV}}^\infty(E). \quad (15)$$

Here, $\Pi_{E_{\min}}^{E_{\max}}(E)$ is 1 between E_{\min} and E_{\max} and 0 otherwise. Fig. 8 shows the detailed balance efficiency with perfectly nonoverlapping absorptions for a GaN host material under a 1-sun 6000-K black-body spectrum, where we find a limiting efficiency of 44%, as previously reported [31]. The efficiency loss from the 48.5% global maximum is due to GaN having too large a bandgap, which could be reduced by considering an

InGaN host material. The white dashed line represents IBSCs. In the lower left region, where $E_{IV} + E_{CI} < E_{CV}$, the device gains more current at a cost of some voltage, leading to an efficiency increase compared with the IBSC.

A working QD IBSC depends on having partially filled IB states, which is controlled by doping or photofilling. The results from Fig. 8 are for perfect nonoverlapping absorptions, but we have added the trajectories showing the energy thresholds of the CR (dashed) and EO (solid) systems as doping changes filling in the IB. In both cases, the trajectories reach the high efficiency-potential region. While this curve makes the CR appear to give highest efficiency at low doping, doping or photofilling to give carriers in the IB is required to make the CI absorption possible in reality. We now consider a more realistic model for the absorptances, including the effects of filling the IB.

For the second absorptance case, we use $a(E)$ obtained from the QD $\mathbf{k}\cdot\mathbf{p}$ model, shown in Fig. 5. To obtain reasonable results, we must find a way to limit $a(E)$ at low E . For materials whose absorptance continues to low energy, as can occur in the CI process because of excitation of thermally excited electrons in the QD states, (10) erroneously gives an infinite emitted photon flux if the voltage exceeds any energy where $a(E)$ is finite. For finite-thickness materials, general cell analysis allows treatment of infinitesimal absorptances in finite-thickness materials, where a population inversion exists, but little stimulated emission is produced in practice [33]. Recent work on absorption in hot carrier solar cells [34] and in the presence of Urbach tails [35] in detailed balance calculations resolved this low-energy absorption problem by treating Pauli exclusion. They found a simple analytic expression to capture the important physics, making $a(E)$ dependent on the quasi-Fermi-level separation between bands. Those works considered only two-band systems, in which the quasi-Fermi levels of each band move away from midgap as the quasi-Fermi level splitting increases. Such behavior does not occur for the two subgap transitions in an IB system. The photofilling or photodepletion of the IB depends crucially on the relative strength of the CI and IV processes and cannot be separately expressed in terms of only μ_{CI} or μ_{IV} [36]. The equivalent analysis for the IB case has not yet been completed. Instead of using either the more complicated general cell analysis or an inconsistent photofilling theory, we use the standard detailed balance method with $a(E)$ clipped to zero for all E below the point where $a(E)=0.01$. With this method, using the absorptions from the $\mathbf{k}\cdot\mathbf{p}$ model, we show in Fig. 9 that the CR system attains a 36% maximum efficiency, which is well above the Shockley–Queisser limit. We note that if we ignore the internal inconsistency of the method of [34] as applied to an IB system, we find that the CR system attains a maximum efficiency of 34%, which is similar to the 36% with our hard cutoffs.

We can achieve higher efficiency by optimizing over the QD geometry and indium fraction. We performed an optimization with the Fermi level fixed such that six electrons occupy the IB states at 0 K. The Fermi level was fixed to reduce the optimization space and to keep the corresponding doping level at a realistic value. The barrier thicknesses in the z and in-plane directions were fixed at 100 Å. Given the fixed barrier, the superlattice

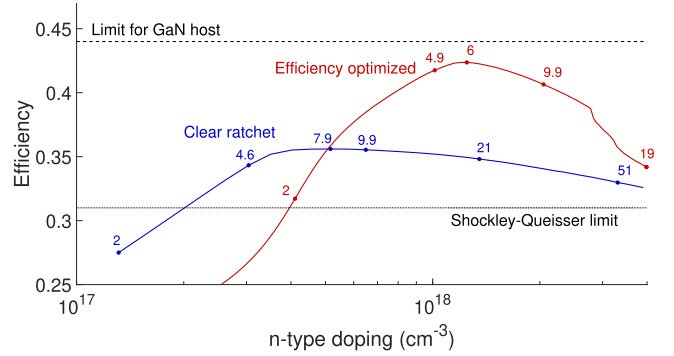


Fig. 9. Detailed balance efficiency as function of doping for the CR (blue) and EO (red) systems with 200 layers of dots. The rise from low doping is due to the increase of CI absorption up to the maximum, where the IV and CI processes are current matched. At larger doping, the CI process overproduces current compared with the IV process, decreasing the efficiency. Numbers along curves indicate the mean number of electrons per dot at 300 K. Dashed line is the detailed balance efficiency limit for a RBSC with a GaN host material and perfect nonoverlapping absorptions under a 1-sun 6000-K black-body spectrum. Dotted line is the Shockley–Queisser limit.

unit cell size varies along with the dot radius and height. Fig. 9 shows that we can achieve an efficiency of 42%, close to the detailed balance limit for systems with a GaN host material. The optimization was converged within a 0.1% efficiency tolerance, using 5149 plane waves. Sensitivity analysis shows an absolute 1% efficiency loss with a 2-Å reduction or 1-Å increase in the radius, an 18-Å decrease or 15-Å increase in height, or a 3% reduction or 1% increase in indium fraction. The corresponding n-type doping level of the system is $1 \times 10^{18} \text{ cm}^{-3}$.

Although the EO system has higher detailed balance efficiency than the CR, it does not have a ratchet. The detailed balance approach only depends on the absorption profiles of the system and has no dependence of the carrier lifetimes one would have in an actual device with nonradiative processes. The optimization produced a system with stronger subgap absorptions, aided by the spatial overlap of the electron and hole states.

The above efficiency analyses included 200 dot layers to enable sufficient optical depth for the CI process in the CR system and an optimistic $\Delta=20$ meV. Fig. 10 shows how the efficiencies change with the number of QD layers and Δ . We find that the CR system is more sensitive to the number of layers, due to its weaker absorption cross sections, as seen in Fig. 4, and in particular the slow rise of $a_{IV}(E)$; the voltage of the ratchet system is limited by E_{IV} but it needs many layers to attain significant absorption in the energy range near E_{IV} . In the case of the EO system, we can decrease the number of layers down to 50–100 and only lose 1%–2% absolute in efficiency. It would also be possible to construct a system somewhere between the two, having a smaller ratchet, but also requiring fewer QD layers to achieve high efficiency. The effects of Δ are stronger on the EO system (which was only optimized for $\Delta=20$ meV), with a significantly reduced efficiency at $\Delta=200$ meV. The CR efficiency depends less strongly on Δ and even increases for larger Δ at some points.

Not explored in the single-particle calculations of this work are the effects of the electric field produced by the spatially

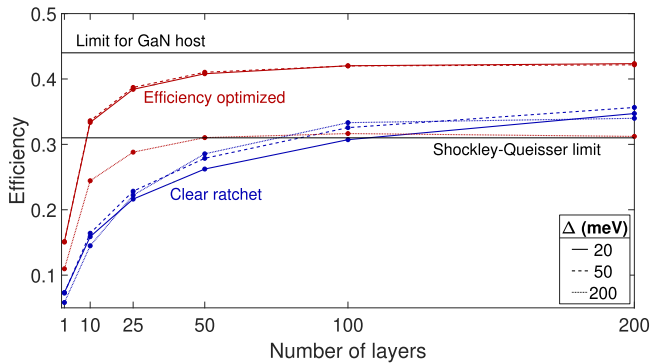


Fig. 10. Detailed balance efficiency of the CR (blue) and EO (red) systems for varying number of QD layers and linewidth broadening Δ . Thin black lines are the Shockley-Queisser limit and the efficiency limit for a RBSC with a GaN host material and perfect nonoverlapping absorptions under a 1-sun 6000-K black-body spectrum. Temperature is 300 K and Fermi level is fixed such that the CR system contains 4.9 electrons per QD and 6.1 for the EO.

separated charges after photoexcitation. This additional electric field should lead to a decrease in the overall potential that separates the states. We also do not consider the effects of either the built-in or external potentials. In this work, we consider an infinite lattice for the electronic structure calculation, making it difficult to explicitly include these potentials, as they would break the periodicity. However, in a standard p-i-n structure and 200 layers of dots, the built-in potential would contribute only about 17 mV of potential change across each dot layer, which is small compared with the piezoelectric potentials seen in Fig. 2. In a p-n-i-p-n-type structure, with QDs in the intrinsic layer, as in [37], there is no built-in potential across the dots. The QD IB states are about 1 eV from the GaN CB band edge, a gap considerably larger than thermal energy.

V. CONCLUSION

In this article, we have presented an example of an experimentally accessible InGaN QD system that can serve as a RBSC. This device uses the piezoelectric potential to spatially separate the lowest electron and hole states to block recombination after the IV optical transition. Blocking this recombination pathway extends the lifetime of the carriers so that they can absorb a second photon for the CI transition.

We also present an optimized system that promises high efficiency if the device were radiatively limited, although actual QD devices generally have strong nonradiative recombination, which makes the ratchet system desirable.

We have calculated the electronic structure of a 3-D InGaN/GaN superlattice of cylindrical QDs and calculated the absorption cross sections for the subgap transitions. To calculate the absorption cross section for the CI transition, we have presented a method that approximates the higher energy states of the host material as bulk $\mathbf{k}\cdot\mathbf{p}$ states. Absorptances were constructed from the cross sections of systems with up to 200 layers of QDs with a Lambertian back reflector. While strong absorption

requires many layers, the ratchet still exists with only one layer and should be measurable.

REFERENCES

- [1] W. Shockley and H. J. Queisser, "Detailed balance limit of efficiency of p-n junction solar cells," *J. Appl. Phys.*, vol. 32, no. 3, pp. 510–519, 1961.
- [2] M. Yoshida, N. J. Ekins-Daukes, D. J. Farrell, and C. C. Phillips, "Photon ratchet intermediate band solar cells," *Appl. Phys. Lett.*, vol. 100, no. 26, 2012, Art. no. 263902.
- [3] A. Luque and A. Martí, "Increasing the efficiency of ideal solar cells by photon induced transitions at intermediate levels," *Phys. Rev. Lett.*, vol. 78, pp. 5014–5017, 1997.
- [4] A. Pusch and N. J. Ekins-Daukes, "Voltage matching, étendue, and ratchet steps in advanced-concept solar cells," *Phys. Rev. Appl.*, vol. 12, 2019, Art. no. 44055.
- [5] E. Z. Zhang and J. J. Krich, "Efficiency limits of electronically coupled upconverter and quantum ratchet solar cells using detailed balance," *J. Appl. Phys.*, vol. 127, no. 21, 2020, Art. no. 213105.
- [6] S. Asahi, H. Teranishi, K. Kusaki, T. Kaizu, and T. Kita, "Two-step photon up-conversion solar cells," *Nature Commun.*, vol. 8, no. 1, 2017, Art. no. 14962.
- [7] A. Vaquero-Stainer *et al.*, "Semiconductor nanostructure quantum ratchet for high efficiency solar cells," *Commun. Phys.*, vol. 1, no. 1, 2018, Art. no. 7.
- [8] T. Sogabe *et al.*, "Experimental demonstration of energy-transfer ratchet intermediate-band solar cell," *Commun. Phys.*, vol. 4, no. 1, 2021, Art. no. 38.
- [9] L. Sang *et al.*, "A multilevel intermediate-band solar cell by InGaN/GaN quantum dots with a strain-modulated structure," *Adv. Mater.*, vol. 26, no. 9, pp. 1414–1420, 2014.
- [10] R. Cheriton *et al.*, "Two-photon photocurrent in InGaN/GaN nanowire intermediate band solar cells," *Commun. Mater.*, vol. 1, 2020, Art. no. 63.
- [11] J. Renard *et al.*, "Evidence for quantum-confined stark effect in GaN/AlN quantum dots in nanowires," *Phys. Rev. B*, vol. 80, 2009, Art. no. 121305.
- [12] L. Robichaud and J. J. Krich, "Efficient Fourier space quantum dot $\mathbf{k}\cdot\mathbf{p}$ for wurtzite systems including smooth alloy profile and spatially varying elastic and dielectric constants," *J. Appl. Phys.*, vol. 129, no. 22, Jun. 2021, Art. no. 224301.
- [13] E. Yablonovitch, "Statistical ray optics," *J. Opt. Soc. Amer.*, vol. 72, no. 7, pp. 899–907, Jul. 1982.
- [14] L. Robichaud and J. J. Krich, "Ingan quantum dot superlattices as ratchet band solar cells," in *Proc. IEEE 48th Photovolt. Specialists Conf.*, 2021, pp. 1626–1630.
- [15] A. D. Andreev and E. P. O'Reilly, "Theory of the electronic structure of GaN/AlN hexagonal quantum dots," *Phys. Rev. B*, vol. 62, no. 23, pp. 15851–15870, 2000.
- [16] S. Tomić, A. G. Sunderland, and I. J. Bush, "Parallel multi-band $\mathbf{k}\cdot\mathbf{p}$ code for electronic structure of zinc blend semiconductor quantum dots," *J. Mater. Chem.*, vol. 16, no. 20, pp. 1963–1972, 2006.
- [17] N. Vukmirović, Z. Ikonić, D. Indjin, and P. Harrison, "Symmetry-based calculation of single-particle states and intraband absorption in hexagonal GaN/AlN quantum dot superlattices," *J. Phys. Condens. Matter*, vol. 18, no. 27, pp. 6249–6262, Jul. 2006.
- [18] N. Vukmirović and S. Tomić, "Plane wave methodology for single quantum dot electronic structure calculations," *J. Appl. Phys.*, vol. 103, no. 10, May 2008, Art. no. 103718.
- [19] M. Winkelnkemper, A. Schliwa, and D. Bimberg, "Interrelation of structural and electronic properties in $\text{In}_x\text{Ga}_{1-x}\text{N}/\text{GaN}$ quantum dots using an eight-band $\mathbf{k}\cdot\mathbf{p}$ model," *Phys. Rev. B*, vol. 74, no. 15, Oct. 2006, Art. no. 155322.
- [20] S. Tomić and N. Vukmirović, "Erratum: Excitonic and biexcitonic properties of single GaN quantum dots modeled by 8-band $\mathbf{k}\cdot\mathbf{p}$ theory and configuration-interaction method [phys. rev. b79, 245330 (2009)]," *Phys. Rev. B*, vol. 86, no. 15, Oct. 2012, Art. no. 159902.
- [21] S. Tomić and N. Vukmirović, "Excitonic and biexcitonic properties of single GaN quantum dots modeled by 8-band $\mathbf{k}\cdot\mathbf{p}$ theory and configuration-interaction method," *Phys. Rev. B*, vol. 79, no. 24, Jun. 2009, Art. no. 245330.
- [22] J. Pal, G. Tse, V. Haxha, M. A. Migliorato, and S. Tomić, "Second-order piezoelectricity in wurtzite III-N semiconductors," *Phys. Rev. B*, vol. 84, Aug. 2011, Art. no. 85211.

- [23] S. Tomić, T. Sogabe, and Y. Okada, "In-plane coupling effect on absorption coefficients of InAs/GaAs quantum dots arrays for intermediate band solar cell," *Prog. Photovolt.: Res. Appl.*, vol. 23, no. 5, pp. 546–558, Feb. 2014.
- [24] S. L. Chuang and C. S. Chang, "k · p method for strained wurtzite semiconductors," *Phys. Rev. B*, vol. 54, pp. 2491–2504, Jul. 1996.
- [25] Z. Ikonic, V. Milanovic, and M. Tadic, "Intersubband optical transition matrix elements for hole states in semiconductor quantum wells," *J. Phys.: Condens. Matter*, vol. 7, no. 35, pp. 7045–7052, Aug. 1995.
- [26] B. Damilano, N. Grandjean, S. Dalmaso, and J. Massies, "Room-temperature blue-green emission from InGaN/GaN quantum dots made by strain-induced islanding growth," *Appl. Phys. Lett.*, vol. 75, no. 24, pp. 3751–3753, 1999.
- [27] J. Ma *et al.*, "Anomalous temperature dependence of photoluminescence in self-assembled InGaN quantum dots," *Appl. Phys. Lett.*, vol. 101, no. 13, 2012, Art. no. 131101.
- [28] G.-E. Weng *et al.*, "Strong localization effect and carrier relaxation dynamics in self-assembled InGaN quantum dots emitting in the green," *Nanoscale Res. Lett.*, vol. 10, no. 1, 2015, Art. no. 31.
- [29] M. Tadić and Z. Ikonić, "Bound-free intersubband absorption in p-type doped semiconductor quantum wells," *Phys. Rev. B*, vol. 52, pp. 8266–8275, Sep. 1995.
- [30] G. Todorović, V. Milanović, Z. Ikonić, and D. Indjin, "The absorption cross section for bound-free transitions in semiconductor quantum dots," *Solid State Commun.*, vol. 110, no. 2, pp. 103–107, 1999.
- [31] L. Robichaud and J. J. Krich, "InGaN quantum dots for intermediate band solar cells," in *Proc. IEEE 46th Photovolt. Specialists Conf.*, 2019, pp. 2138–2142.
- [32] P. Wurfel, "The chemical potential of radiation," *J. Phys. C: Solid State Phys.*, vol. 15, no. 18, pp. 3967–3985, Jun. 1982.
- [33] M. A. Green, "Single junction cells," in *Proc. 3rd Gener. Photovolt.: Adv. Sol. Energy Convers.*, 2003, pp. 35–58.
- [34] D.-T. Nguyen *et al.*, "Quantitative experimental assessment of hot carrier-enhanced solar cells at room temperature," *Nature Energy*, vol. 3, no. 3, pp. 236–242, 2018.
- [35] J. Wong, S. T. Omelchenko, and H. A. Atwater, "Impact of semiconductor band tails and band filling on photovoltaic efficiency limits," *ACS Energy Lett.*, vol. 6, no. 1, pp. 52–57, Jan. 2021.
- [36] R. Strandberg and T. W. Reenaas, "Photofilling of intermediate bands," *J. Appl. Phys.*, vol. 105, no. 12, 2009, Art. no. 124512.
- [37] A. Marti, L. Cuadra, and A. Luque, "Quasi-drift diffusion model for the quantum dot intermediate band solar cell," *IEEE Trans. Electron Devices*, vol. 49, no. 9, pp. 1632–1639, Sep. 2002.